PHYSICS AND CHEMISTRY OF SOLID STATE
V. 23, No. 1 (2022) pp. 101-112
Section: Physics

DOI: 10.15330/pcss.23.1.101-112

Vasyl Stefanyk Precarpathian National University

ФІЗИКА І ХІМІЯ ТВЕРДОГО ТІЛА
Т. 23, № 1 (2022) С. 101-112
Фізико-математичні науки

PACS: 81.05.ue, 61.10.Nz, 68.37.Hk, 87.64.Je, 81.20.−n ISSN 1729-4428

M. Panigrahi[1], B. Avar[2]

Synthesis and Characterization of Binary Reduced Graphene Oxide/Metal Oxide Nanocomposites

[1]*School of Mechanical Engineering, Vellore Institute of Technology, Chennai–600127, Tamil Nadu, India, mrutyunjayjapan@gmail.com*
[2]*Department of Metallurgical and Materials Engineering, Zonguldak Bülent Ecevit University, Incivez, 67100 Zonguldak, Turkey, barisavar@beun.edu.tr*

Graphene/metal oxide composites have generated interest for a variety of applications, such as energy storage, catalysts, and electronics, etc. However, one of the primary technical barriers to real applications has been the lack of practical and environmentally benign synthesis methods for producing homogenous graphene/metal oxide nanocomposites on a wide scale. Therefore, a simple, efficient, and environmentally friendly approach to the synthesis of graphene (reduced graphene oxide: rGO)/metal oxide (MO) nanocomposites was developed with the chemical reaction of graphene oxide (GO) and various metal oxide powders under mild temperature conditions. In this study, the GO was synthesized from graphite powder using modified Hummer's technique initially. Later, using ascorbic acid (AA) as a reducing agent, various binary nanocomposites such as rGO/ZnO, rGO/CuO, rGO/TiO_2, and rGO/Ag_2O were synthesized by in situ approach. The structural and surface properties of the synthesized binary nanocomposites were extensively examined by X-ray diffraction (XRD), Field emission scanning electron microscopy (FESEM), Energy dispersive spectroscopy (EDX), and Raman spectroscopy techniques. The XRD analysis of the synthesized binary rGO/MO nanocomposites confirmed the nanocrystalline nature. However, the FESEM and EDX analysis substantiated the MO nanoparticles were uniformly distributed onto the rGO layers anchoring of MO onto rGO particles and interacted with the rGO residual functional groups. Raman spectroscopy analysis indicated the increased number of defects because of the interfacial interaction between rGO and MO and the formation of binary rGO/MO nanocomposites.

Keywords: Binary nanocomposites, rGO/ZnO, rGO/CuO, rGO/TiO_2, rGO/Ag_2O, XRD, SEM, EDX, Raman analysis

Received 9 December 2021; Accepted 4 March 2022.

Introduction

The research of carbon nanostructures is very comprehensive because of their incomparable properties and diverse applications. Amid the disparate specialty of carbon, graphene is one of the most popular materials in the current generation because of its exceptionally magnificent properties. Graphene is an allotrope of carbon comprising of a single atomic thick sheet of graphite with honeycomb lattice nanostructure [1]. It possesses superb electronic, physical, thermal, chemical stability, mechanical, biocompatibility, and tribological properties. It has a young's modulus of 1 TPa, fracture toughness of 42 N/m, intrinsic strength of 130 GPa, and specific surface area of 2620 m^2/g, respectively. It also has a very high electronic conductivity at ambient temperature, its electron mobility is 2.5×10^5 cm^2/Vs, and thermal conductivity of around 3000 Wm/K, respectively [2, 3].

Although the graphene material presents unique properties, the insoluble graphene has restricted its usages without functionalizing metal oxides [4]. The oxidized form of graphene, graphene oxide (GO) has received substantial recognition for investigation in numerous aspects of materials science/engineering with many different possible usages. The GO has textural and structural properties that enable to find numerous applications in the functional devices, such as energy

storage, solar and fuel cells, supercapacitors, photoreduction, battery materials, nanofluids, adsorption, Al-based composites, filtration systems, and drug delivery etc. [5, 6].

Graphene and its derivatives consisting of GO have been considered as one of the most promising applicants for the growth of efficient photocatalytic composite materials. However, rGO has novel properties that can revolutionize the performance of functional devices. The rGO hybrids can be constructed with transition metal oxides to improve energy storage applications. Because of the large surface area, simplicity of surface modification, and exceptional thermal and mechanical stability, graphene has recently been recognized as a supporting material [7].

Various synthesis methods for GO have been reported. The most prominent methods are mechanical exfoliation, chemical vapor deposition (CVD), SiC pyrolysis, e-beam evaporation, Hummers and Offeman technique, and modified Hummer's technique, and so on [2, 5]. The synthesis of graphene has been most widely used by the Hummers and Offeman technique, which produces GO and that is reduced using chemical or thermal methods to form graphene or reduced graphene oxide (rGO).

Carbon materials have unique properties such as chemical inactivity and stability in both acidic and basic environments [8]. However, the tunable textural and chemical properties of different materials can be assigned to produce composites with MO. Further, the modification of graphene's physicochemical characteristics is critical for the development of graphene-based composite materials [9]. However, synergistic interactions between rGO and the materials bonded to its surface are frequently responsible for the better performance of graphene-based composites. As a result, the quality of the graphene-based materials used will have a significant impact on the final nanocomposite's performance. Graphene-based nanocomposites have been used to generate innovative adsorbents and photocatalysts in the environmental field. At the same time, most pure MOs suffer from certain limitations such as low conductivity, chemical instability, and mechanical brittleness [9]. To overcome this, it is necessary to combine with rGO to create a suitable composite with notable electrical and mechanical characteristics such as wide surface area and strong chemical stability.

Zinc oxide (ZnO) is one of the environmentally friendly semiconductor materials that can be used as a photocatalyst because of its property of a wide energy bandgap of 3.37 eV [10-13]. It creates an adequate amount of electrons and holes upon illumination that facilitates the degradation of certain pollutants. ZnO has a high exciton binding energy of 60 meV, allowing it to be used in electrochemical properties, magnetic compounds, solar cells, and gas sensing devices, among other things [13]. However, ZnO has poor electrical conductivity, its pseudo-capacitance behavior, and it corrodes when exposed to light, limiting its practical application. In this context, several attempts have been made to improve carrier concentrations provide an alternative carrier pathway, and reduce charge recombination by regulating ZnO with other functional materials, such as GO and rGO [3, 4, 7, 10-24].

Similarly, cupric oxide (CuO) has a bandgap of 1.2 eV [25]. Therefore, in photocatalytic activity, this might be an important advantage over a broad bandgap since sunlight can be fully utilized. Regardless of this, CuO's photocatalytic efficiency is low because of the extremely high recombination rate of photogenerated electron-hole pairs. Therefore, the loading of CuO on rGO can be used to enhance photocatalytic efficacy [25-31].

Likewise, titanium dioxide (TiO_2) is utilized in a large variety of applications such as catalysts due to its high oxidizing power, energy, and the environment because of easy availability, chemical stability, good optical and electronic properties [8, 9, 32-39]. However, low quantum performance because of the recombination of electron-positive hole pairs is a measure limitation [32, 35-38]. Therefore, efforts have been made to develop TiO_2-based composite substances capable of reducing electron-positive hole recombination. At the same time composites of TiO_2 with graphene, the family has been specified as a highly efficient photocatalyst in air and water purification [9].

In the same way, silver oxide (Ag_2O) is a semiconductor material that is regarded to be the most suitable for large-scale applications due to its low energy bandgap [39]. At the same time, Ag_2O nanoparticles have the advantages of easy preparation, low cost, and wide application. Because of its good electrical conductivity, chemical stability, and fast redox reaction, the incorporation of Ag_2O into the rGO network can increase the specific capacitance. [31, 39-45].

The GO/MO nanocomposites have a higher specific surface area compared to the GO [2]. This leads to improved gas detection efficiency and properties of the oxidation-reduction reaction that occurs on the surface of the MO and alters the charge carriers. The rGO/MO nanocomposites can be synthesized in various ways depending upon the MO loading/rGO modification, such as ex-situ and in situ techniques.

The ex-situ technique includes the prior synthesis of MO nanomaterials in the required morphology and dimensions and subsequently connected to the surface of the functionalized rGO. The functionalization step is most vital to increase the solubility of rGO and the synthesis of GO/MO nanocomposites. However, the in-situ technique includes the formation of MO nanomaterials in the presence of functionalized rGO. The GO/MO nanocomposites are commonly synthesized in a simultaneous reduction of GO and metal precursors ($Zn(NO_3)_26H_2O$, $Cu(NO_3)_23H_2O$, $AgNO_3$, and TiO_2, etc.) with the reductants ($NaBH_4$, amino acid, and $N_2H_4.H_2O$, etc.) [5]. The in-situ technique is the most commonly used plan for the synthesis of rGO/MO nanocomposites. In this technique, the use of protecting surfactants or extra linker molecules can be avoided. Apart from the above advantage, a range of chemical and physical synthesis techniques can be employed such as hydrothermal/solvothermal, solution chemistry, direct precursor decomposition, gas-phase deposition, sol-gel, and template techniques, etc. Given the above, the in-situ technique was implemented in the current research.

Finding an appropriate reducing agent, which can be

utilized to synthesize rGO is of great importance. The reductants such as $NaBH_4$, amines, and $N_2H_4.H_2O$, etc. have been used by many researchers in the past. It was found that hydrazine hydrate ($N_2H_4.H_2O$) is the best reductant in the case of producing rGO sheets with good electrical conductivity. However, a green reduction technique has been introduced as the toxic nature of hydrazine to the environment and to the living organisms as well. Therefore, several alternatives such as $NaBH_4$, amino acid, organic acid, plant extract, sugar, antioxidants, and microorganisms, etc. have been utilized in research. Among all the above, ascorbic acid (AA) is considered as an alternative reducing agent for GO which is a mild reductive ability and is most environmentally friendly [5, 46, 47]. Apart from this, the physical property such as electrical conductivity of AA-rGO is similar or higher to that obtained from hydrazine-rGO. It may also be essential as a capping reagent in the stabilization of rGO sheets simultaneously. The AA-rGO can be used for various applications such as sensors, flexible graphene fibers, and dye-sensitized solar cells, etc. The removal of O-functional groups is relatively easy and performs the reduction in a short duration while using a small amount of AA. Therefore, the present study focused on the synthesis of GO from graphite powder using modified Hummer's technique initially. Later, the binary rGO/ZnO, rGO/CuO, rGO/TiO_2, and rGO/Ag_2O nanocomposites were synthesized with the chemical reduction of GO and investigated their structural and surface properties in detail.

Experimental details

1.1. Chemicals

Graphite powder (CDH, > 99.5 %, particle size 50 µm), sulfuric acid (H_2SO_4: Merck, ~98 %), potassium permanganate ($KMnO_4$: Rankem, 99 %), hydrogen peroxide (H_2O_2: Fluka, 30 vol %), distilled water (H_2O: Milli-Q), and hydrochloric acid (HCl: Sigma Aldrich, ~37 wt%) were used in this study. All chemicals used in this study were analytical-grade reagents and used in as received condition without any further purification.

1.2. Synthesis of graphene oxide (GO)

Graphene oxide (GO) was initially synthesized by a modified Hummer's technique. The preparation steps of GO from graphite powder using modified Hummer's technique consists of three steps (Figure 1). The oxidation and exfoliation of graphite powder were used for synthesizing GO using modified Hummer's technique. The first step was the low-temperature stage, in which, 3 g of graphite powder was added gradually to a reactor containing 70 mL of concentrated H_2SO_4 as an intercalating agent under the magnetic stirring condition at below 20 °C. The mixture was magnetically stirred for 30 minutes. The second step was the medium temperature stage, where 9 g of $KMnO_4$ was slowly added to the solution as an oxidizing agent keeping the temperature under 45 °C. The oxidation process was conducted for 3 hours. The distilled water (150 mL) was added dropwise to the solution and followed by the instant addition of 500 mL. The third step was the high-temperature stage, where the temperature was increased to 95 °C for 15 minutes. Further, the suspension was cooled to below 20 °C after removing the ice bath from the process followed by the addition of 15 mL of H_2O_2. Generally, the H_2O_2 and distilled water were used for exfoliation assistant of the GO layers. The water suspension of the obtained GO was kept for sedimentation. The purifying process was carried out with a custom-made microfiltration system. The GO was washed several times with HCl (10 %) and distilled water for ~20 minutes each at 5000 rpm. Then the filtrate was dried overnight in the air and later heated in a vacuum oven at 35 °C for 12 hours to remove the moisture. Finally, the dry GO powder was obtained and kept in a glove box.

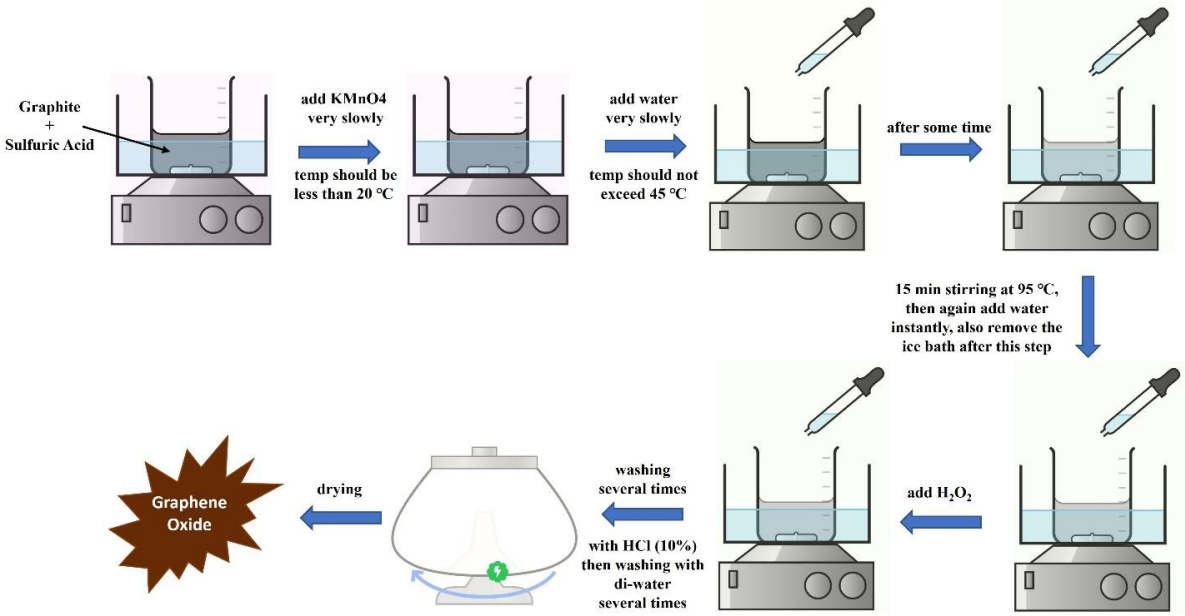

Fig. 1. Modified Hummer's techniques for synthesizing GO from graphite powder.

The yield of GO synthesized was calculated using the below equation [47]: Yield = $[m_f/m_i] \times 100$ %, where, m_f = Mass of the final product (g) and m_i = Mass of feed-in

(g)

1.3. Synthesis of reduced graphene oxide (rGO) and binary rGO/MO nanocomposites

The reduced graphene oxide (rGO) was synthesized from GO using the chemical reduction technique. Several techniques have been reported for the synthesis of GO-based nanocomposites. In the current research, rGO/ZnO nanocomposite was synthesized through immediate simple reduction of GO and Zinc Nitrate Hexahydrate [$Zn(NO_3)_2H_2O$] using a reducing agent. The reducing agent used in these current experiments was Ascorbic Acid (AA). In a typical synthetic protocol, 0.5 g of the synthesized GO was dissolved in 100 mL of deionized water (DI) in a beaker. The obtained mixture was then sonicated for 40 minutes at 45 Amp for homogeneous suspension. In a separate beaker, 6.83 g of [$Zn(NO_3)_2H_2O$] was dissolved in 100 mL of DI. The above mixture was added dropwise in the GO suspension under sonicated conditions and the reaction mixture was further sonicated for 1 hr to homogenize the resulting mixture. The AA (4.0437 g) was then added to the obtained mixture and set up reflux at 80 ºC for 24 hr. After removing the reflux, the rGO/ZnO nanocomposite was filtered and washed with DI several times. The rGO/ZnO nanocomposite was then stored in the glove box for characterization and analysis purposes. Similarly, the rGO/CuO, rGO/TiO_2, and rGO/Ag_2O nanocomposites were synthesized with the reduction of GO and Copper Nitrate Trihydrate [$Cu(NO_3)_23H_2O$], GO and Silver Nitrate ($AgNO_3$), and GO and Titanium Dioxide (TiO_2), respectively.

1.4. Characterization of the Nanocomposites

The prepared GO, rGO, and the rGO/ZnO, rGO/CuO, rGO/TiO_2, and rGO/Ag_2O nanocomposites were characterized using X-ray diffraction (XRD), Field emission scanning electron microscopy (FESEM), X-ray spectrometer (EDX), and Raman spectroscopy techniques. The XRD patterns were recorded by a Panalytical Empyrean powder diffractometer with Cu kα radiation (λ = 0.154 Å). The recorded XRD patterns were obtained from 5° to 60° (2θ). The morphology and the local chemical analysis of the samples were performed with ZEISS Supra 55 FESEM and Oxford Instruments EDX. The Raman study was carried out using Princeton Instruments Acton SP2750 excited with a laser at a wavelength of 514 nm.

Results and Discussion

2.1 Structural Characterization

Figure 2 shows the XRD patterns of graphite powder, GO, rGO, and binary rGO/ZnO, rGO/CuO, rGO/TiO_2, rGO/Ag_2O nanocomposites, respectively. The crystalline structure of carbon materials such as graphite is generally investigated by X-ray structural analysis, which permits the determination of the structure's degree of order and the size of the crystallites (the smallest structural components).

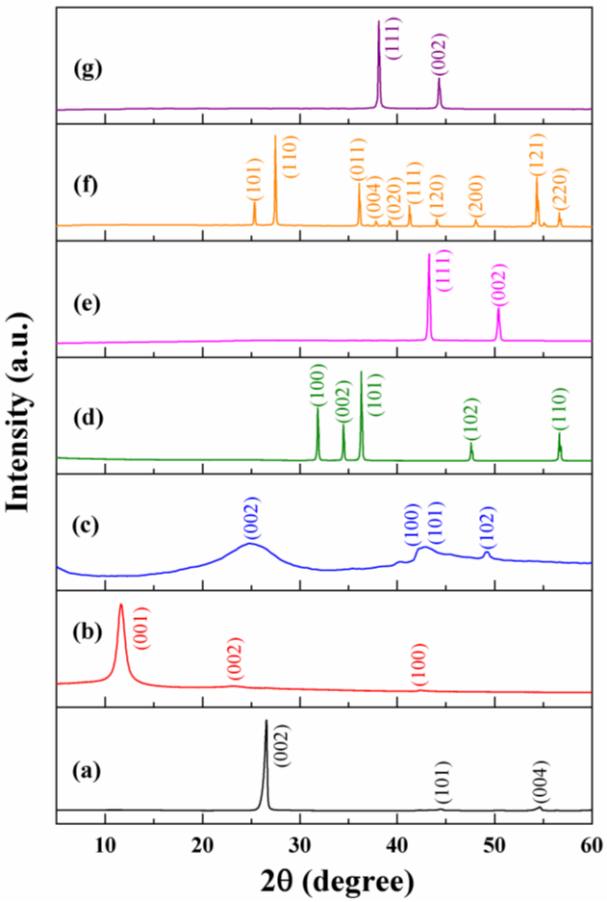

Fig. 2. XRD patterns of (a) graphite, (b) GO, (c) rGO, and binary (d) rGO/ZnO, (e) rGO/CuO, (f) rGO/TiO_2, and (g) rGO/Ag_2O nanocomposites.

The graphite consists of a laminar array of carbon atoms at the vertices of regular hexagons. Each adjacent layer is shifted relative to its predecessor by the interatomic distance. Therefore, the structure of graphite is best characterized by the inter-plane distance, which depends on the conditions in which the graphite was produced [48]. The phase heterogeneity and structural order of the graphite samples were investigated by X-ray structural analysis and described by the resolution of the reflexes from the corresponding crystallographic planes.

Figure 2 (a) exhibits the X-ray diffraction pattern of the as-received graphite powder sample. The reflex (002) for which 2θ ≈ 26.5º was very highly crystalline intense. It corresponds to an inter-plane distance (d) of 0.34 nm and (004) is of higher-order for which 2θ ≈ 54.6º, are reflections from polyarene layers. The graphite phases were identified using the JCPDS card no. of 41-1487. Based on the XRD pattern, the interplane distance d_{hkl} for the sample was calculated using Bragg's law, which is shown in equation (1) as [48]:

$$d_{hkl} = \lambda/2sin\theta\ , \qquad (1)$$

where, λ is the radiation wavelength and θ is the reflection angle for the reflex (hkl).

The reflex (101) for which 2θ ≈ 44.6º, determines the longitudinal dimension L_a of the structural elements. As the reflexes in the diffraction pattern are asymmetric, it probably indicates the presence of several carbon phases

(substructures) with different degrees of order and structural characteristics. Figures 2 (b) and (c) exhibit the XRD pattern of the GO sample which was synthesized by the modified Hummers technique and the rGO sample obtained from the GO using chemical reduction technique. From the XRD pattern (Figure 2 (b) and (c)), it is clearly seen the difference between GO and rGO samples and were identified using the JCPDS card No. of 82-2261 and 75-1621, respectively. The XRD pattern of GO exhibits a strong diffraction peak of $2\theta \approx 44.6^{o}$, corresponding to the (001) reflex with an inter-plane distance of 0.73 nm. The increase of inter-plane distance from 0.34 nm (for graphite powder) to 0.73 nm (GO) was because of the introduction of the various O-containing functional groups (C=O, C−OH, and COOH, etc.) on the surface of GO, confirming the oxidation process, hence, it facilitates the hydration and exfoliation of GO sheets in aqueous media [1, 2, 5, 6, 46, 47, 49]. Apart from the above strong diffraction peak (001), the other two low diffraction peaks of $2\theta \approx 23.3^{o}$ and 42.6^{o} correspond to the (002) and (100) reflexes which were seen in the XRD patterns. In the rGO sample (Figure 2 (c)), the peak that exists at 12.1^{o} was disappeared, which characterizes the reduction process and indicates the efficient exfoliation of the multiple layers during the chemical reduction of the GO [2]. It was observed that the formation of a broad peak because of the lack of crystallinity of rGO, appeared at $2\theta \approx 25.2^{o}$ which corresponds to the (002) reflex with an inter-plane distance of 0.35 nm. Based on the XRD results, the structural changes were occurred in the rGO samples. The inter-plane distance of the rGO sample (0.35 nm) was slightly larger than that of the graphite powder (0.34 nm). Apart from the above broad diffraction peak (002), the other three low diffraction peaks of $2\theta \approx 42.3^{o}$, 43.2^{o}, and 49.4^{o}, correspond to the (100), (101), and (102) reflexes which were seen in the XRD patterns. The XRD patterns of the binary rGO/ZnO nanocomposite (Figure 2 (d)) show the clear sharp peaks, suggesting the very good crystallinity of the synthesized ZnO. The characteristic peaks appeared at $2\theta \approx 31.8^{o}$, 34.3^{o}, 36.4^{o}, 47.5^{o}, and 56.8^{o}, which corresponds to the (100), (002), (101), (102), and (110) reflexes, respectively. This corresponds to a ZnO hexagonal wurtzite phase (JCPDS card no. 98-018-0052) [3, 12, 20-22]. The diffraction peak ($2\theta \approx 56.8^{o}$) corresponds to the (110) reflex, which was observed to have a higher intensity which suggests that the thickness of ZnO was probably increased for this sample. However, the diffraction peaks of rGO which were observed at $2\theta \approx 25.2^{o}$ correspond to the (002) reflex did not appear, probably because the diffraction peak of ZnO nanocrystals is much stronger than (002) of rGO [4]. The average crystallite size was estimated using Scherrer equation (2) as [32, 37]:

$$D = 0.9\lambda/\beta_{1/2}cos\theta, \qquad (2)$$

where, λ is the characteristic X-ray wavelength applied and $\beta_{1/2}$ is the half-width of the peak at the 2θ value.

The XRD patterns of binary rGO/CuO nanocomposite (Figure 2 (e)) show very good sharp peaks, which indicate a high degree of crystallinity. The prominent peaks appeared at $2\theta \approx 43.2^{o}$ and 50.4^{o}, which corresponds to the (111) and (002), reflexes, respectively. All the peaks of rGO/CuO nanocomposites clearly show the cubic system of Cu (JCPDS card No. 98-005-3757). However, there were no obvious characteristic peaks of rGO in the binary rGO/CuO nanocomposites, which is probably because of the strong Cu peaks covering the rGO peaks [28]. Similarly, the XRD patterns of binary rGO/TiO_2 nanocomposite (Figure 2 (f)) shows the sharp crystallinity characteristic peaks appeared at $2\theta \approx 25.4^{o}$, 27.5^{o}, 36.1^{o}, 37.9^{o}, 39.3^{o}, 41.1^{o}, 43.9^{o}, 47.9^{o}, 54.3^{o}, and 56.8^{o}, which corresponds to the (101), (110), (011), (004), (020) (111), (120), (200), (121), and (220), reflexes, respectively. The synthesized binary rGO/TiO_2 nanocomposite shows a diffraction pattern corresponding to tetragonal rutile (JCPDS card No. 98-016-7961) and tetragonal anatase (JCPDS card No. 98-004-4882) phases. There was no separate peak for rGO detected in the binary rGO/TiO_2 nanocomposite, possibly because of the low amount and low intensity of rGO [35, 37, 38]. It was understood that the dispersion of TiO_2 nanoparticles on the surface of rGO or the crystallization and phase structure of TiO_2 nanoparticles was not greatly affected by the addition of rGO in the binary rGO/TiO_2 nanocomposite [36]. Likewise, the XRD pattern of binary rGO/Ag_2O nanocomposite is shown in Figure 2 (g). Two intense diffraction peaks appeared at $2\theta \approx 37.9^{o}$ and 44.3^{o}, corresponding to the (111) and (002) reflexes, which confirmed the cubic Ag (JCPDS card No. 98-005-3761) phases. The rGO peak was not detected in the binary rGO/Ag_2O nanocomposite, probably due to the prominent peaks of crystalline Ag [45].

2.2 Morphological Characterization

Figure 3 shows the SEM micrographs of the graphite powder, GO, rGO, and binary rGO/ZnO, rGO/CuO, rGO/TiO_2, and rGO/Ag_2O nanocomposites samples, respectively. The low and high magnification SEM micrographs of the graphite powder sample (Figure 3 (a, a')) show the thin plate stacked structure. Figure 3 (b, b') shows the SEM micrographs of the low and high magnifications of the GO samples. The micrograph shows wrinkles and folds structure [1, 5, 6]. It shows the flaky texture results in its layered microstructure without any amorphous particles which are due to the interaction of O-containing functional groups present on the surface [1]. The SEM micrographs (low and high magnification) of rGO obtained from GO are shown in Figure 3 (c, c'). The micrographs show wrinkled surfaces with distinct edges and folding nanosheets [47]. This is due to the rapid removal of O-containing functional groups in GO and the exfoliation of the GO layers during the ultrasonic treatment process in aqueous media [1]. Figure 3 (d, d') shows the SEM micrographs of the binary rGO/ZnO nanocomposites. It was observed that the particle size of the rGO was reduced in the binary rGO/ZnO nanocomposites. The high agglomeration of the particles shows that the anchoring of ZnO onto rGO particles by interacting with the residual functional groups of rGO

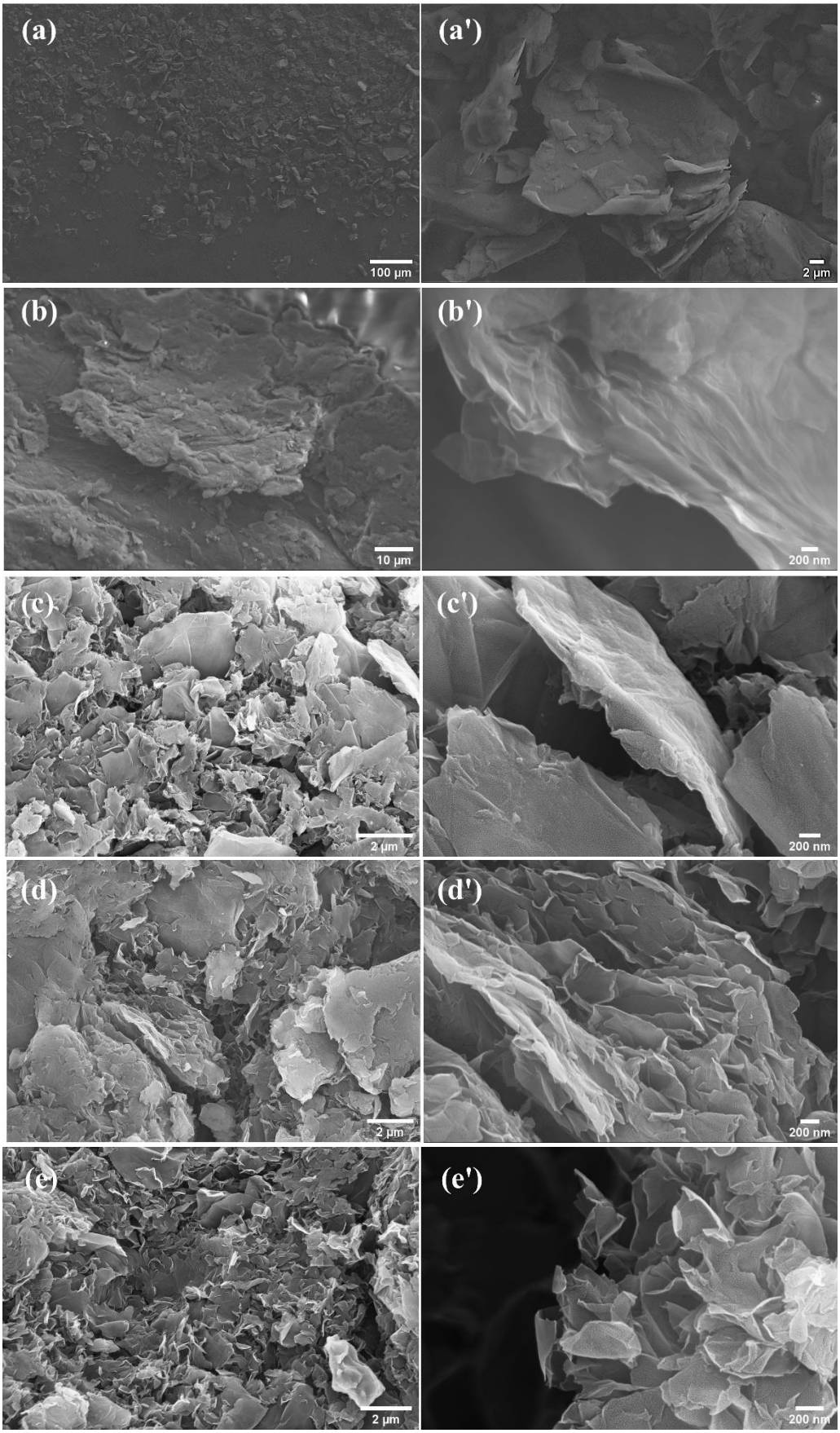

Fig. 3. SEM micrographs of the samples; (a, a') graphite, (b, b') GO, (c, c') rGO, and binary (d, d') rGO/ZnO, (e, e') rGO/CuO, (f, f') rGO/TiO_2, (g, g') rGO/Ag_2O (left: low-magnification, right: high-magnification) (continued on the next page).

Fig. 3. (continuation)

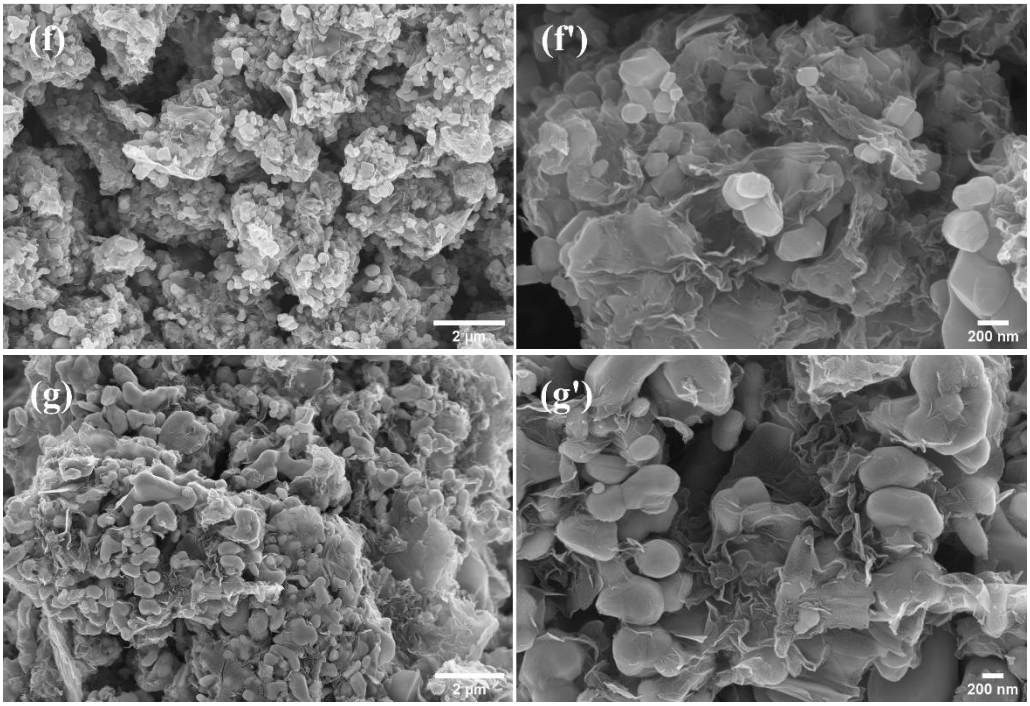

(continuation)

Fig. 3. SEM micrographs of the samples; (a, a') graphite, (b, b') GO, (c, c') rGO, and binary (d, d') rGO/ZnO, (e, e') rGO/CuO, (f, f') rGO/TiO_2, (g, g') rGO/Ag_2O (left: low-magnification, right: high-magnification).

and suggesting the formation of rGO-ZnO nanocomposites [16, 18, 22]. Similarly, the SEM micrographs of the rGO/CuO binary nanocomposites are shown in Figure 3 (e, e'). It shows that the Cu particles were agglomerated and homogeneously distributed [26]. However, the morphology of binary rGO/CuO nanocomposites was in the form of flakes [25-27]. In the same way, the SEM micrograph of the binary rGO/TiO_2 nanocomposite is shown in Figure 3 (f, f'). It was observed that the agglomeration of TiO_2 nanoparticles covering the GO and the wrinkling of the rGO sheets were consistent with the morphologies [38]. The TiO_2 particles were found to be spherical with a size ~400 nm. Likewise, the SEM micrograph of the binary rGO/Ag_2O nanocomposite is shown in Figure 3 (g, g'). It was observed that the agglomerated irregular particles, where the Ag particles impregnated over the rGO [39]. However, the Ag particles were observed to be spherical with a size of ~200 nm.

The EDAX was used to analyze the oxidation states and the elemental or chemical composition of the synthesized rGO sample and binary rGO/ZnO, rGO/CuO, rGO/TiO_2, and rGO/Ag_2O nanocomposite samples. The results of the EDAX analysis along with SEM micrographs are shown in Figure 4. The EDAX spectrum of the synthesized rGO (Figure 4 (a)) indicates the presence of high concentrations of carbon (C) and oxygen (O) of 82.35 and 17.65 at%, respectively. The presence of O in the structure of rGO indicates that the reduction of GO to rGO [27]. The high amount of C contents in the rGO indicates that the reduction process of O-containing functional groups [32]. The non-identified spectrum detected was probably because of the impurity present which was from the chemical reaction process. Figure 4 (b) exhibits the EDAX spectrum along with the SEM micrographs of binary rGO/ZnO nanocomposite sample. The binary rGO/ZnO nanocomposite is composed mainly of C, O, and Zn elements with 79.96, 19.79, and 0.24 at%, respectively. Similarly, the EDAX pattern of the prepared binary rGO/CuO nanocomposite is shown in Figure 4 (c). The presence of C, O, and Cu elements of 81.58, 14.39, and 4.03 at% in the prepared binary rGO/CuO nanocomposite were observed. Figure 4 (d) shows the EDAX analysis of binary rGO/TiO_2 nanocomposite sample with 35.51 at% of C, 52.01 at% of O, and 12.48 at% of Ti, respectively. This confirms the TiO_2 nanoparticles were uniformly distributed onto the rGO layers. Likewise, the EDAX spectrum of the binary rGO/Ag_2O nanocomposite sample is shown in Figure 4 (e). It was found that the binary rGO/Ag_2O nanocomposite contents 67.88 at% of C, 21.61 at% of O, and 10.52 at% of Ag, respectively. Therefore, it was concluded that the composition of O and the metals (Zn, Cu, Ti, and Ag) are originated from the respective metal oxide (ZnO, CuO, TiO_2, and Ag_2O) nanoparticles, whereas the C, mainly from the rGO. It was also observed that some non-identified spectrum detected in each binary nanocomposites confirms the impurity present, which was obtained from the chemical reaction process.

Raman Spectroscopy is an extensively used non-destructive chemical analysis approach that gives exhaustive information about the phase, chemical structure, crystallinity, and molecular interactions of C-based materials [1, 2, 6]. It is based upon the interaction of light with the chemical bonds inside a particular material. The prime features in the Raman spectra of graphite (carbon-based materials) are represented by the D, G, and 2D peaks. Figure 5 (a) shows the Raman spectra of the as-received graphite powder sample.

The two most intensive peaks are the G band and the 2D band located at 1565 cm^{-1} and 2718 cm^{-1}, respectively. The graphite powders displayed a small D band located at 1341 cm^{-1}. The G band is because of the bond stretching of all pairs of sp^2 atoms in both the rings and chains [2]. It is the outcome of in-plane optical vibrations and corresponds to the optical E_{2g} phonons produced at the Brillouin zone center by the bond stretching of sp^2 carbon pairs in both rings and chains [1, 2]. The D band is because of the first-order resonance and the arising of the breathing mode of aromatic rings, which indicates the defects or edges in the graphite powder sample [2]. Therefore, the intensity of the D-band is frequently used as a measure of the degree of

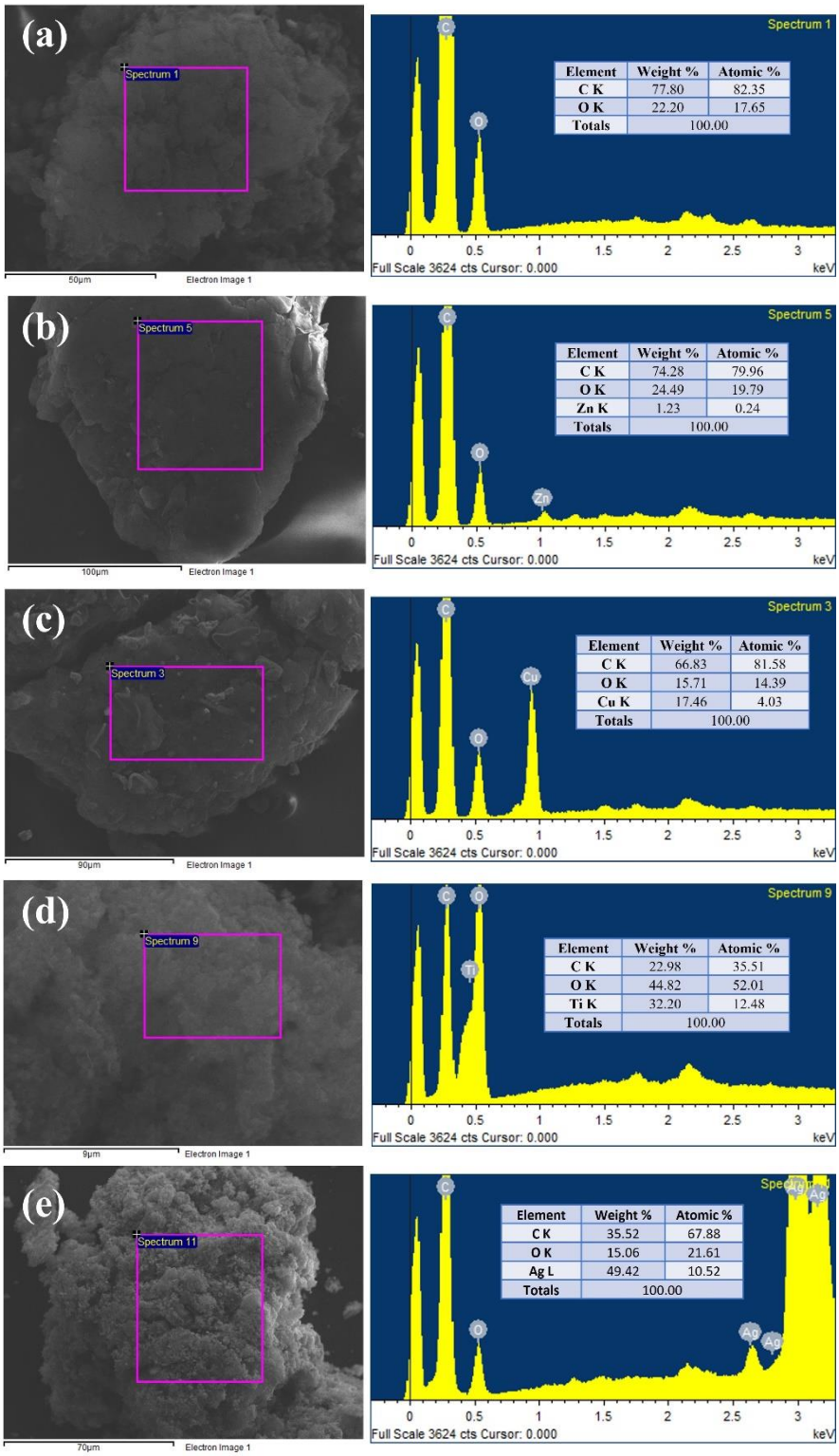

Fig. 4. EDAX spectrum with SEM micrograph of (a) rGO and binary (b) rGO/ZnO, (c) rGO/CuO, (d) rGO/TiO_2, and (e) rGO/Ag_2O nanocomposites.

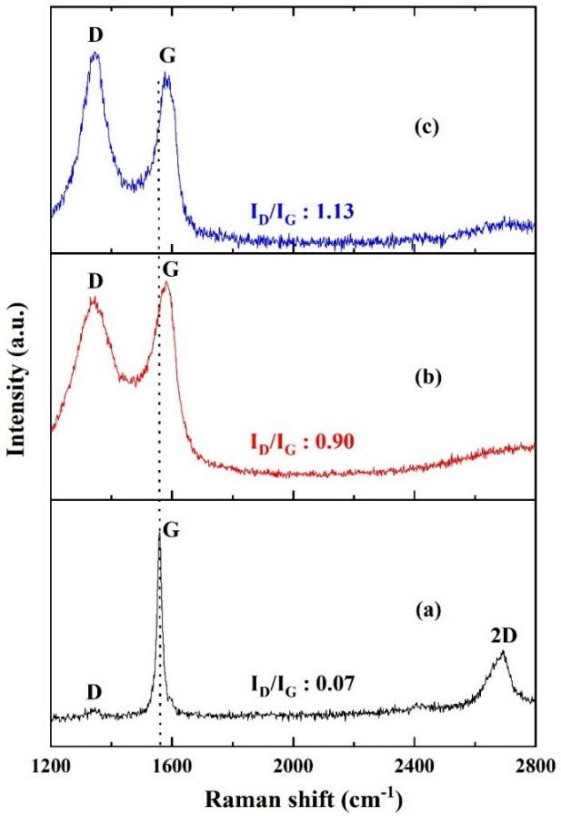

Fig. 5. Raman spectra of (a) graphite, (b) GO, and (c) rGO samples.

disorder. The 2D band (G' band) is the overtone of the D band, the second foremost band in the Raman spectra, and is invariably noticed in graphite powder samples [6]. All kinds of sp^2 carbon materials exhibit a strong peak around 2700 cm^{-1} in the Raman spectra [2, 6, 46]. The 2D-band is a second-order two-phonon process and exhibits a strong frequency dependence on the excitation laser energy. The intensity ratio (I_D/I_G = 0.07) of the D band (1341 cm^{-1}) to that of the G band (1565 cm^{-1}) is a measure of disorder degree and the average size of the sp^2 domains in graphite powder samples. Since the 2D band is structure sensitive, it clearly shows the transition from crystalline to an amorphous phase in GO and rGO samples upon the oxidation process. Similarly, the Raman spectra of GO in Figure 5 (b) exhibit the appearance of a strong intensity of the D band located at 1353 cm^{-1} with intensity concerning that of the G band located at 1600 cm^{-1}. Likewise, the Raman spectra of rGO in Figure 5 (c) indicate the existence of a very strong intensity of the D band located at 1388 cm^{-1} with intensity concerning that of the G band located at 1612 cm^{-1}. The intensity of the D band along with a large bandwidth indicates that the important structural disorder in GO and rGO materials, respectively. This can also attribute to the formation of defects and disorders such as the presence of in-plane hetero-atoms, grain boundaries, aliphatic chain, etc [6]. It was also observed that the Raman spectra of GO and rGO samples (Figure 5 (b) and (c)) show significant changes, where the G band was shifted towards a higher wavenumber (1600 cm^{-1} in case of GO and 1612 cm^{-1} in case of rGO) due to the oxidation of graphite. At the maximum oxidation state, the G band reaches a position at 1612 cm^{-1} (Figure 5 (c)). The shift in G-band is attributed to the generation of new sp^3 carbons in the graphite lattice [6]. Furthermore, the full width half maximum (FWHM) of the G-band is also increased relative to the oxidation level [6]. Because the 2D band is very sensitive to the stacking order of the graphite along the c-axis, it is commonly used to estimate the structural parameters of the c-axis orientation [6]. Severe chemical oxidation is expected to result in major structural changes in the graphite lattice due to the formation of different types of O-functional groups in the basic plane and at the edges [20]. The varnishing of the 2D band intensity is because of the breaking of the stacking order because of the oxidation reaction [44]. The intensity ratio (I_D/I_G) of 0.90 and 1.13 in the case of GO and rGO samples (Figure 5 (b) and (c)) confirms the reduction of GO and rGO samples. This is also due to an increase in edge planes and a decrease in the size of in-plane sp^2 domains, as well as the formation of defects and disorders in GO and rGO samples [23].

The Raman spectra of binary rGO/ZnO, rGO/CuO, rGO/TiO_2, and rGO/Ag_2O nanocomposites are shown in Figure 6. The structural changes from GO to rGO/ZnO nanocomposite are reflected in the Raman spectra, which are shown in Figure 6 (a). From Figure 6 (a), it was noticed the existence of two strong intensities of the D band located at 1494 cm^{-1} with intensity concerning that of the G band located at 1965 cm^{-1}. However, the D band and G band were located at 1353 cm^{-1} and 1600 cm^{-1}, respectively in the case of GO (Figure 6 (b)). The shifting of the Raman spectrum indicates the charge transfer between rGO and ZnO. Besides, the intensity ratio (I_D/I_G) was enhanced from 0.90 to 1.17 compared

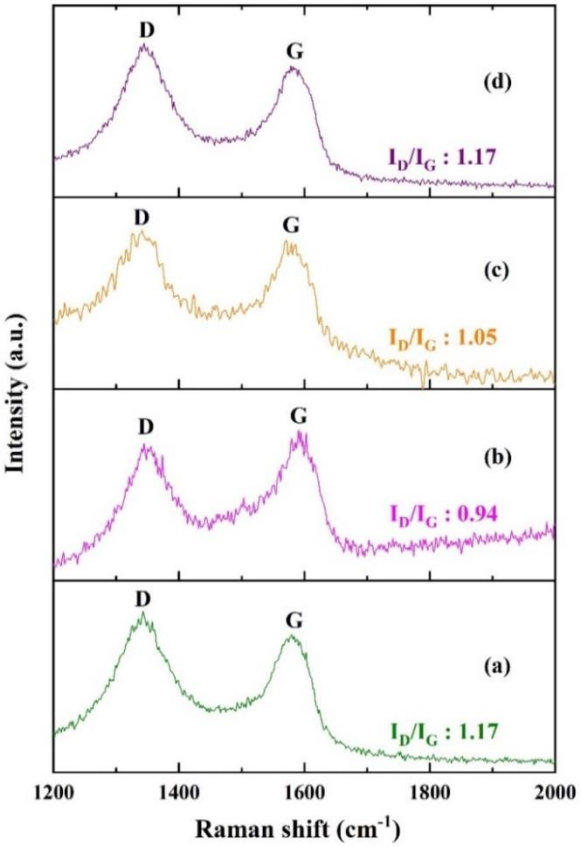

Fig. 6. Raman spectra of binary (a) rGO/ZnO, (b) rGO/CuO, (c) rGO/TiO_2, and (d) rGO/Ag_2O nanocomposites.

with GO, suggesting the formation of rGO and rGO/ZnO

composite. This also indicates the growing numbers of defects are created owing to interfacial interaction between rGO and ZnO [14, 16]. Similarly, the structural changes from GO to rGO/CuO nanocomposites are shown in the Raman spectra (Figure 6 (b)). It was noticed that the D band was detected at 1518 cm^{-1} and the G band detected at 2012 cm^{-1} and the intensity ratio was also increased to 0.94. Likewise, the structural changes from GO to rGO/TiO_2 nanocomposites are shown in the Raman spectra (Figure 6 (c)). It was revealed that the D band was detected at 1506 cm^{-1} and the G band detected at 1977 cm^{-1} and the I_D/I_G ratio was also increased to 1.05. In addition, the structural changes from GO to rGO/Ag_2O nanocomposites are shown in the Raman spectra (Figure 6 (d)). It was detected that the D band was observed at 1530 cm^{-1} and the G band was observed at 2024 cm^{-1} and the I_D/I_G ratio was also increased to 1.17.

Conclusion

The graphene oxide powders were successfully synthesized by modified Hummer's technique. The results indicated that the graphite powder was successfully oxidized to highly oxygenated and exfoliated GO sheets. The chemical reduction of GO was performed using ascorbic acid as a green reductant, which is the most environmentally friendly. The structural and morphological change of reduced graphene oxide powder was perceived using various analytical instruments. Binary rGO/ZnO, rGO/CuO, rGO/TiO_2, and rGO/Ag_2O nanocomposites with different wt. percentages of GO were successfully synthesized using a chemical reduction method with an in-situ technique. The XRD patterns confirmed the successful synthesis of the binary nanocomposites. Furthermore, the peaks of the binary rGO/ZnO and rGO/TiO_2 nanocomposite show the hexagonal wurtzite of ZnO and tetragonal rutile and anatase of TiO_2 phases, respectively. However, the peaks of the binary rGO/CuO and rGO/Ag_2O nanocomposite show the cubic system of Cu and Ag, respectively. The SEM micrograph showed the high agglomeration of the particles by interacting with the residual functional groups of rGO in the binary nanocomposites. The elemental composition values measured using the EDAX and the nominal composition values proposed for this study were almost close to each other. The reduction of GO and defects present in the binary nanocomposites was primarily substantiated by the Raman analysis.

Acknowledgements

This work was supported by the Scientific Research Projects Coordination Unit of Zonguldak Bülent Ecevit University, project no. 2017-73338635-02.

Panigrahi M. **–** Doctor of Engineering, Faculty of School of Mechanical Engineering
Avar B. **–** Doctor of Science, Associate Professor of Department of Metallurgical and Materials Engineering

[1] W.C. Oh, F.J. Zhang, Asian Journal of Chemistry 23(2), 875 (2011); https://asianjournalofchemistry.co.in/User/ViewFreeArticle.aspx?ArticleID=23_2_98.
[2] S.N. Alam, N. Sharma, L. Kumar, Graphene 6, 1 (2017); https://doi.org/10.4236/graphene.2017.61001.
[3] A.P. Benevides, A.R. Campos, L.C. Vieira, C.R. Perez, D.V. Cesar, Materials Research 23(1), e20190580 (2020); https://doi.org/10.1590/1980-5373-MR-2019-0580.
[4] R. Ramadan, S.K. Abdel-Aal, Journal of Materials Science: Materials in Electronics 32, 19667 (2021); https://doi.org/10.1007/s10854-021-06489-y.
[5] K. Kanishka, H. De Silva, H.H. Huang, M. Yoshimura, Applied Surface Science 447, 338 (2018); https://doi.org/10.1016/j.apsusc.2018.03.243.
[6] K. Krishnamoorthy, M. Veerapandian, K. Yun, S.J. Kim, Carbon 53, 38 (2013); https://doi.org/10.1016/j.carbon.2012.10.013.
[7] U.C. Rajesh, J. Wang, S. Prescott, T. Tsuzuki, D.S. Rawat, ACS Sustainable Chemistry & Engineering 3(1), 9 (2015); https://doi.org/10.1021/sc500594w.
[8] H.M. Aziz, M.H.K. Al-Mamoori, L.H. Aboud, Journal of Physics: Conference Series 1818, 012206 (2021); https://doi.org/10.1088/1742-6596/1818/1/012206.
[9] R. Zouzelka, M. Remzova, J. Plsek, L. Brabec, J. Rathousky, Catalysts 9, 708 (2019); https://doi.org/10.3390/catal9090708.
[10] F.C. Romeiro, M.A. Rodrigues, L.A.J. Silva, A. C. Catto, L.F. da Silva, E. Longo, E. Nossol, R.C. Lima, Applied Surface Science 423, 743 (2017); https://doi.org/10.1016/j.apsusc.2017.06.221.
[11] S.K. Mandal, K. Dutta, S. Pal, S. Mandal, A. Naskar, P.K. Pal, T.S. Bhattacharya, A. Singha, R. Saikh, S. De, D. Jana, Materials Chemistry and Physics 223, 456 (2019); https://doi.org/10.1016/j.matchemphys.2018.11.002.
[12] R.T. Ngaloy, A.M. Fontanilla, M.S.R. Soriano, C.S. Pascua, Y. Matsushita, I.J.A. Agulo, Journal of Nanotechnology 1895043 (2019); https://doi.org/10.1155/2019/1895043.
[13] S. Kar, K. Chakraborty, T. Pal, S. Ghosh, AIP Conference Proceedings 2265, 030134 (2019); https://doi.org/10.1063/5.0017186.
[14] L. Zhang, X. Zhang, G. Zhang, Z. Zhang, S. Liu, P. Li, Q. Liao, Y. Zhao, Y. Zhang, RSC Advances 5, 10197 (2015); https://doi.org/10.1039/C4RA12591F.
[15] C. Rodwihok, D. Wongratanaphisan, Y.L.T. Ngo, M. Khandelwal, S. H. Hur, J. S. Chung, Nanomaterials 9, 1441 (2019); https://doi.org/10.3390/nano9101441.

[16] A.S. Merlano, F.R. Pérez, R. Cabanzo, E. Mejía, L.M. Hoyos, Á. Salazar, Journal of Physics: Conference Series 1541, 012015 (2020); https://doi.org/10.1088/1742-6596/1541/1/012015.
[17] H. Gao, Y. Ma, P. Song, J. Leng, Q. Wang, Journal of Materials Science: Materials in Electronics 32, 10058 (2021); https://doi.org/10.1007/s10854-021-05664-5.
[18] J. Jayachandiran, J. Yesuraj, M. Arivanandhan, A. Raja, S. Austin Suthanthiraraj, R. Jayavel, D. Nedumaran, Journal of Inorganic and Organometallic Polymers and Materials 28, 2046 (2018); https://doi.org/10.1007/s10904-018-0873-0.
[19] Z. Zhan, L. Zheng, Y. Pan, G. Sun, L. Li, J. Mater. Chem. 22, 2589 (2012); https://doi.org/10.1039/C1JM13920G.
[20] S. Kumar, R.D. Kaushik, G.K. Upadhyay, L.P. Purohit, Journal of Hazardous Materials 406(15), 124300 (2021); https://doi.org/10.1016/j.jhazmat.2020.124300.
[21] P. Dhandapani, M.S. AlSalhi, R. Karthick, F. Chen, S. Devanesan, W. Kim, A. Rajasekar, M. Ahmed, M.J. Aljaafreh, A. Muhammad, Journal of Hazardous Materials 409, 124661 (2021); https://doi.org/10.1016/j.jhazmat.2020.124661.
[22] Z. Alves, C. Nunes, P. Ferreira, Nanomaterials 11, 2149 (2021); https://doi.org/10.3390/nano11082149.
[23] S. Meti, M.R. Rahman, M.I. Ahmad, K.U. Bhat, Applied Surface Science 451, 67 (2018); https://doi.org/10.1016/j.apsusc.2018.04.138.
[24] M. Sreejesh, S. Dhanush, F. Rossignol, H.S. Nagaraja, Ceramics International 43(6), 4895 (2017); https://doi.org/10.1016/j.ceramint.2016.12.140.
[25] S. Sagadevan, J.A. Lett, G.K. Weldegebrieal, S. Garg, W.C. Oh, N.A. Hamizi, M.R. Johan, Catalysts 11, 1008 (2021); https://doi.org/10.3390/catal11081008.
[26] K. Revathi, S. Palantavida, B.K. Vijayan, Materials Today: Proceedings 9, 587 (2019); https://doi.org/10.1016/j.matpr.2018.10.379.
[27] S. Siddique, Z. Abdin, M. Waseem, T. Naseem, A. Bibi, M. Hafeez, S.U. Din, S. Haq, S. Qureshi, Journal of Inorganic and Organometallic Polymers and Materials 31, 1359 (2021); https://doi.org/10.1007/s10904-020-01760-x.
[28] Y. Wang, Z. Wen, H. Zhang, G. Cao, Q. Sun, J. Cao, Catalysts 6, 214 (2016); https://doi.org/10.3390/catal6120214.
[29] R. Eivazzadeh-Keihan, R. Taheri-Ledari, M. S. Mehrabad, S. Dalvand, H. Sohrabi, A. Maleki, S. M. Mousavi-Khoshdel, A.E. Shalan, Energy Fuels 35, 10869 (2021); https://doi.org/10.1021/acs.energyfuels.1c01132.
[30] A.B. Alayande, M. Obaid, I.S. Kim, Materials Science & Engineering C 109, 110596 (2020); https://doi.org/10.1016/j.msec.2019.110596.
[31] Sridevi, B. Balraj, N. Senthilkumar, G.K.D. Prasanna Venkatesan, Journal of Superconductivity and Novel Magnetism 33, 3501 (2020); https://doi.org/10.1007/s10948-020-05594-z.
[32] M. Ruidíaz-Martínez, M.A. Álvarez, M.V. López-Ramón, G. Cruz-Quesada, J. Rivera-Utrilla, M. Sánchez-Polo, Catalysts 10, 520 (2020); https://doi.org/10.3390/catal10050520.
[33] R.K. Nainani, P. Thakur, Water Science & Technology 73(8), 1927 (2016); https://doi.org/10.2166/wst.2016.039.
[34] S.W. Bokhari, A.H. Siddique, X. Yue, H. Singh, M.D. Hayat, W. Gao, International Journal of Energy Research 44(14), 12197 (2020); https://doi.org/10.1002/er.5864.
[35] M.S.A.S. Shah, A.R. Park, K. Zhang, J.H. Park, P.J. Yoo, ACS Applied Materials & Interfaces 4, 3893 (2012); https://doi.org/10.1021/am301287m.
[36] L. Yu, L. Wang, X. Sun, D. Ye, Journal of Environmental Sciences 73, 138 (2018); https://doi.org/10.1016/j.jes.2018.01.022.
[37] Y. Liu, RSC Advances 4, 36040 (2014); https://doi.org/10.1039/C4RA06342B.
[38] J.F. Leal, S.M.A. Cruz, B.T.A. Almeida, V.I. Esteves, P.A.A.P. Marques, E.B.H. Santos, Environmental Science: Water Research & Technology 6, 1018 (2020); https://doi.org/10.1039/C9EW00950G.
[39] H. Xiao, T. Wang, Journal of Physics and Chemistry of Solids 154, 110100 (2021); https://doi.org/10.1016/j.jpcs.2021.110100.
[40] N. Meng, S. Zhang, Y. Zhou, W. Nie, P. Chen, RSC Advances 5, 70968 (2015); https://doi.org/10.1039/C5RA13574E.
[41] S.A. Bhat, M.A. Rather, S.A. Pandit, P.P. Ingole, M.A. Bhat, Analyst 140, 5601 (2015); https://doi.org/10.1039/C5AN00740B.
[42] M. Iqbal, Z. Abdin, T. Naseem, M. Waseem, S.U. Din, M. Hafeez, S. Haq, S. Qureshi, A. Bibi, S.U. Rehman, R. Hussain, Journal of Inorganic and Organometallic Polymers and Materials 31, 100 (2021); https://doi.org/10.1007/s10904-020-01680-w.
[43] T. Jiao, H. Guo, Q. Zhang, Q. Peng, Y. Tang, X. Yan, B. Li, Scientific Reports 5, 11873 (2015); https://doi.org/10.1038/srep11873.
[44] S. Sinha, N.A. Devi, S. Nongthombam, R. Bhujel, S. Rai, G. Sarkar, B.P. Swain, Diamond & Related Materials 107, 107885 (2020); https://doi.org/10.1016/j.diamond.2020.107885.
[45] M. Sharma, M.K. Patra, S.K. Jain, Journal of Nanostructures 9(3): 547 (2019); https://doi.org/10.22052/JNS.2019.03.016.

[46] J. Zhang, H. Yang, G. Shen, P. Cheng, J. Zhang, S. Guo, Chemical Communications 46, 1112 (2010); https://doi.org/10.1039/B917705A.
[47] Y.T. Khoo, International Journal of Engineering Applied Sciences and Technology 5(4), 1 (2020); https://ijeast.com/papers/1-12,Tesma504,IJEAST.pdf.
[48] A.N. Popova, Coke and Chemistry 60(9), 361 (2017) (https://doi.org/10.3103/S1068364X17090058).
[49] Ahmad, J.E. McCarthy, A. Baranov, Y.K. Gun'ko, Materials 8, 5953 (2015); https://doi.org/10.3390/ma8095284.

М. Паніграхі[1], Б. Авар[2]

Синтез та характеристика бінарних відновлених нанокомпозитів оксид графену/оксид металу

[1] Школа машинобудування, Технологічний інститут Веллор, Ченнаї–600127, Таміл Наду, Індія, mrutyunjayjapan@gmail.com
[2]Кафедра металургії та інженерії матеріалів, університет Зонгулдак Бюлент Еджевіта, Інчівез, 67100 Зонгулдак, Туреччина, barisavar@beun.edu.tr

Композити графен / оксид металу викликають значний інтерес через різноманітні застосування, такі як зберігання енергії, каталізатори, електроніка тощо. Однак, однією із основних технічних перешкод для реального застосування була відсутність практичних та екологічно безпечних методів синтезу для виробництва гомогенних нанокомпозитів графен/оксид металу у великому масштабі. Відповідно, було розроблено простий, ефективний та екологічно чистий підхід до синтезу нанокомпозитів графену (відновленого оксиду графену: rGO)/оксиду металу (MO) за допомогою хімічних реакцій оксиду графену (GO) та різних порошків оксиду металу при помірних температурах. У цьому дослідженні GO спочатку синтезують з графітового порошку за допомогою модифікованої техніки Хаммера. Пізніше, використовуючи аскорбінову кислоту (AK) як відновник, різні бінарні нанокомпозити, такі як rGO/ZnO, rGO/CuO, rGO/TiO2 та rGO/Ag2O, їх синтезовано методом in situ. Структурні та поверхневі властивості синтезованих бінарних нанокомпозитів детально досліджено методами дифракції рентгенівських променів (XRD), польової емісійної скануючої електронної мікроскопії (FESEM), енергодисперсійної спектроскопії (EDX) та раманівської спектроскопії. Рентгенофазовий аналіз синтезованих бінарних нанокомпозитів rGO/MO підтвердив нанокристалічну природу. Однак, аналіз FESEM та EDX показав, що наночастинки MO рівномірно розподілені по шарах rGO, які закріплювали MO на частинках rGO та взаємодіяли із залишковими функціональними групами rGO. Аналіз раманівської спектроскопії вказав на збільшення кількості дефектів через міжфазну взаємодію між rGO та MO та утворення бінарних нанокомпозитів rGO/MO.

Ключові слова: бінарні нанокомпозити, rGO/ZnO, rGO/CuO, rGO/TiO_2, rGO/Ag_2O, XRD, SEM, EDX, раманівський аналіз.